Viscoelastic homogenization of 3D woven composites with damping validation in temperature and verification of scale separation

Florian Conejos [a,b], Etienne Balmes [b,c,*], Bastien Tranquart [a], Eric Monteiro [b], Guillaume Martin [c]

[a] Safran Composites, 33 Avenue de la Gare, 91760 Itteville, France
[b] Laboratoire PIMM, Arts et Metiers Institute of Technology, CNRS, Cnam, HESAM Universite, 151 Boulevard de l'Hopital, 75013 Paris, France
[c] SDTools, 44 Rue Vergniaud, 75013 Paris, France

A B S T R A C T

Estimation of damping can be of great importance for turbomachines, where vibration based instabilities like flutter occur. The paper discusses a numerical method to predict the homogenized viscoelastic behavior of 3D woven composites, used in fan blades, from elementary constituent behavior. Yarn and weave microstructures are considered in a two scale homogenization. The matrix and fibers are considered homogeneous with linear viscoelastic and elastic behavior respectively. Temperature and frequency dependence of matrix properties are characterized by complex moduli. Confrontation of numerical predictions with modal damping of a modified Oberst experiment, for a temperature range of −40 to 120 °C, gives good results in terms of absolute value and trends. The homogenization is formulated using matrix operations, which enables the simple use of model reduction techniques for parametric studies on temperature and leads to energy fraction analyses useful to gain understanding of how different components of the constitutive laws contribute to damping and change with temperature. Finally, since weaving patterns have a scale of a few centimeters, that is not small compared to gradients found in the experiment, exact solutions for responses to regular volume loads are used to characterize the validity of the scale separation hypothesis as a function of wavelength.

Contents

1. Introduction

Use of composites, after having increased in aircraft structure for the past decades, is now making its way into engines as well. For example, the LEAP composite fan blade makes use of a 3D woven composites for their design flexibility and high mechanical performance, especially for impact. But building less fuel consuming engines, that operate in high-performance ranges, also implies the need to increase margins for the flutter phenomenon, a structural dynamic instability, by controlling modal damping. Predicting composite damping from constituent properties is thus a critical step.

Review papers [1–3] analyze damping properties of composite materials, by experimental characterization or finite element computation, in order to identify the mechanisms and take them into account in the design and analysis stages. The viscoelastic nature of the matrix, the interphase, the damage, the weaving ondulation, the geometry of the mesostructure, the orientation, the nature of the reinforcement, the hybridization with highly damped materials or systems are listed as sources of dissipation. But, outside non desirable damage, these correspond to a combination of viscoelastic dissipation and geometric effects of the microstructure that enhance this dissipation. The paper will thus focus on viscoelastic homogenization, using illustrations for the case of 3D woven composites whose matrix and fibers are considered homogeneous with respectively linear viscoelastic and elastic behavior.

The will to increase the damping has long been a research subject in composites materials. At the microscale, recent studies show that the shape of the inclusion and the properties of interphase also has an impact on the stiffness and damping of the homogenized cell [4]. At the mesoscale, [5] shows that the mesoscale architecture of the textile composite has a strong influence on its damping for the frequencies that were studied.

The charaterization of the dynamic mechanical properties of a viscoelastic material corresponds to the measurement of a complex modulus [6,7] that dependent on frequency and temperature. Complex modulus can also be obtained through time domain relaxation tests, leading to Prony series representations which are equivalent to the generalized Maxwell frequency domain model [8,9]. Numerically, using this complex modulus is also referred to as exploiting the correspondence principle between linear elasticity and linear viscoelasticity.

The first homogenization approaches considering linear viscoelastic materials were developed in the 1960s [10,11]. More recently for 3D woven composites, homogeneization was performed in time by [12,13] to study the effect of manufacturing residual stress on shapes and [14] to study the influence of temperature.

Homogenization estimate the effective macroscopic properties of a medium seen as heterogeneous at a low scale. The main variations [15] are associated with the choice of boundary conditions applied to the representative volume element (RVE). The nature of 3D woven composite requires a multiscale approach to obtain yarn then weave properties illustrated in Fig. 1. Many reviews summarizing methods for the multiscale analysis of composites can be found [16–19] with broad categories being analytical, semi-analytical or computational homogenization techniques like self consistent scheme, variational formulation, transformation fields analysis or finite element (FE) approaches. This paper focuses on a purely numerical method with a multiscale finite element model.

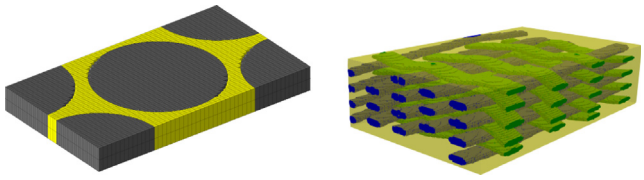

Fig. 1. Finite element models for micro (yarn) and meso (weave) scales.

Homogenization assumes a scale separation between the wavelength, the RVE size and the size of heterogeneities inside the RVE. The study [20] for instance details the impact of RVE choices on homogenization results. In the considered case the weaving pattern length can be significant compared to blade dimensions, so that the scale separation assumption is not necessarily verified. Introducing generalized continuous media of the Cosserat type, or second gradient [21,22] in order to better account for the strong gradients at microscopic level is a known but costly option. So that the focus will be on determining the scale separation validity.

Section 2 addresses homogenization. The classic objective of obtaining equal work for homogeneous and heterogeneous media is developed using matrix formulations that are adapted for optimized implementation of parametric studies in a finite element setting. For the viscoelastic case, the dependence of properties on temperature and frequency is shown to correspond to the weighted sum of real matrices with coefficients corresponding to the complex components of constitutive material stiffness matrix depending on temperature and frequency. Equality of stored and dissipated energy is then used to obtain homogenized properties using simple matrix expressions. Illustrations for the 3D interlock woven composite shown in Fig. 1, consider evolution of storage moduli and loss factors with temperature and demonstrate the notable impact of matrix property changes with temperature, relative moduli of matrix and fibers and geometry of the microstructure.

Weave patterns of 3D composites can be quite large and the experiment detailed in Section 4 will be shown to have gradient lengths that do not verify the scale separation hypothesis. Thus a methodology is developed in Section 3 to quantify the accuracy of homogenized properties by comparing stored and dissipated energies for regular volume loads of arbitrary wavelength. Using periodic solutions [23,24], these can be evaluated exactly assuming a geometrically periodic medium, meaning a cell repeated indefinitely in space.

Finally, to make sure that the proposed viscoelastic homogenization is valid, predictions are confronted with test results in Section 4. Measuring low damping at low frequencies on stiff samples is a challenge so that a modified Oberst setup is considered. After discussing the experimental difficulties, the FEM model of the experiment is analyzed to gain an understanding of the expected damping contributions and spatial distribution of dissipation. The final comparison of the predicted modal damping of two bench modes gives very good results in terms of absolute value and trends of evolution with temperature.

All computations and post-processing were performed in Structural Dynamics Toolbox (SDT) [25].

2. Viscoelastic homogenization using complex modulus

The homogenization approaches developed in this paper use standard techniques expressed with a matrix formulation adapted for FEM computation.

2.1. Elastic homogenization

The classical approach for homogenization is to use the work equality between the homogeneous and heterogeneous media, also known as the Hill Mandel Lemma [26,27], where the strain energy computed for the heterogeneous medium, noted with the h exponent, is equal to the energy computed at the macroscopic level or homogeneous level noted with m,

$$\int_V \{\sigma^m\}^T \{\varepsilon^m\} dV = \int_V \{\sigma^h\}^T \{\varepsilon^h\} dV \tag{1}$$

with σ and ε respectively the stress and strain, and V the domain of the RVE.

Limiting the details to the Kinematic Uniform Boundary Conditions (KUBC) approach, explained for example in [15], a displacement field is imposed at all poi ts belonging to the boundaries of a RVE. The six homogeneous fields $u_k^m\}$, with k indicating the load case, applied on the faces of the volume are

$$[\{u_k^m\}] = \left[\begin{Bmatrix} u_{1\,k}^m \\ u_{2\,k}^m \\ u_{3\,k}^m \end{Bmatrix}\right] = \begin{bmatrix} x & 0 & 0 & 0 & z/2 & y/2 \\ 0 & y & 0 & z/2 & 0 & x/2 \\ 0 & 0 & z & y/2 & x/2 & 0 \end{bmatrix} \tag{2}$$

where the subscript $i \in [1,2,3]$ corresponds to the direction of displacement along each of the coordinates axis x, y and z respectively. These displacement fields correspond to the integration of a unit infinitesimal strain

$$\begin{aligned}[\{\varepsilon_k^m\}] &= \left[\frac{1}{2}(\nabla\{u_k^m\} + \nabla^T\{u_k^m\})\right] \\ &= [I] = \left[\begin{Bmatrix} \varepsilon_{11\,k}^m \\ \varepsilon_{22\,k}^m \\ \varepsilon_{33\,k}^m \\ 2\varepsilon_{23\,k}^m \\ 2\varepsilon_{13\,k}^m \\ 2\varepsilon_{12\,k}^m \end{Bmatrix}\right] = \begin{bmatrix} 1 & 0 & 0 & 0 & 0 & 0 \\ 0 & 1 & 0 & 0 & 0 & 0 \\ 0 & 0 & 1 & 0 & 0 & 0 \\ 0 & 0 & 0 & 1 & 0 & 0 \\ 0 & 0 & 0 & 0 & 1 & 0 \\ 0 & 0 & 0 & 0 & 0 & 1 \end{bmatrix}\end{aligned} \tag{3}$$

Thus, for an homogeneous macroscopic medium, since the strain is given by $\{\varepsilon_k^m\} = \{I_k\}$, the stress $\{\sigma_k^m\}$ corresponding to each loading is found using the generalized Hooke's law or using Voigt notation as

$$\{\sigma_k^m\} = [C^m]\{\varepsilon_k^m\} \tag{4}$$

The work of the homogeneous medium is written

$$\frac{1}{|V|}\int_V \{\varepsilon_k^m\}^T \{\sigma_l^m\} dV = \{I_k\}^T \{\sigma_l^m\} = C_{kl}^m \tag{5}$$

with $|V|$ the total volume of the RVE and C_{kl}^m corresponding to the kl^{th} component of the matrix $[C^m]$, the matrix representation of the material stiffness tensor.

The equivalence is obtained by computing the heterogeneous solution with displacement Eq. (2) imposed on volume faces and enforcing equality of work between the homogeneous and heterogeneous solutions for the fields $\{u_k^m\}|_{nodes}$ which corresponds to the field $\{u_k^m\}$ discretized to each node of the finite element model.

Other boundary conditions such as periodic boundary condition (PBC) or a homogeneous mixed field controlled in displacement (MUBC) detailed in [28] also lead to a direct computation of the material stiffness matrix [29]. Static uniform boundary condition (SUBC), apply a stress, which leads to the compliance matrix that is inverted to obtain the stiffness matrix.

In a finite element setting, the displacement field $\{u\}$ is described by the kinematic degree of freedom (DOF) field called $\{q\}$. For the heterogeneous solution, the known displacement fields Eq. (2) are only enforced at the model nodes belonging to the RVE boundaries denoted with the I index

$$\{q_{I\,k}^h\} = \{q_{I\,k}^m\} = \{u_k^m\}|_{nodes} \tag{6}$$

The static equilibrium in absence of volume forces is defined by the following matrix system

$$\begin{bmatrix} K_{II}^h & K_{IC}^h \\ K_{CI}^h & K_{CC}^h \end{bmatrix} \begin{Bmatrix} q_I^h \\ q_C^h \end{Bmatrix} = \begin{Bmatrix} R_I \\ 0 \end{Bmatrix} \tag{7}$$

where R_I corresponding to reaction forces at RVE boundaries. Degrees of freedom are divided into complementary (interior) and interface groups denoted respectively with C and I indices. A static solution is found for the complementary degrees of freedom by solving

$$\{q_C^h\} = -[K_{CC}^h]^{-1}[K_{CI}^h]\{q_I^h\} \tag{8}$$

which leads to the approximation of a statically admissible stress state.

The link between strain and displacement is defined using the classical notation $\{\varepsilon_k^h\} = [B]\{q_k^h\}$ [30], with $[B]$ the differential operator matrix applied to the shape functions and $\{q_k^h\}$ the vectors fields of degrees of freedom associated with the heterogeneous medium. The stresses are only known at integration points and the heterogeneous work Eq. (5) can be rewritten as

$$\begin{aligned}\int_V \{\varepsilon_k^h\}^T \{\sigma_l^h\} &\approx \sum_g \{\varepsilon_k^h\}^T [C^h]\{\varepsilon_l^h\} w_g J_g \\ &= \{q_k^h\}^T \left(\sum_g [B]^T [C^h][B] w_g J_g\right)\{q_l^h\} \\ &= \{q_k^h\}^T [K^h]\{q_l^h\}\end{aligned} \tag{9}$$

with J_g the determinant of the jacobian matrix associated with each quadrature point g, w_g the quadrature weight and $[K^h]$ the linear elastic stiffness matrix of the heterogeneous medium. The application of Eq. (1) gives

$$[C^m]_{6\times 6} = \frac{[q^h]_{6\times N}^T [K^h]_{N\times N} [q^h]_{N\times 6}}{|V|} \tag{10}$$

with N the number of degrees of freedom of the system.

While, this expression does not change the classical result, where work can be computed at integration point level asking the FEM software to extract strain and stress fields [15], the matrix expression shown here notably simplifies implementation and extension to parametric reduced models [31] which will be used to reduce the cost of temperature and frequency dependence studies. Restricting the basis learning phase to computations at two temperatures, as in the classical multimodel reduction introduced in [31], is not detailed but used in this paper. At the mesoscale, a computation at one temperature for a 3D woven composites mesostructure of around 1.5 millions of DOF lasts 6 000s. Reduction lasts 13 000s and computation at 100 temperatures 28 000s, or a factor 15 speedup.

2.2. Benchmark

The implementation has been benchmarked against available solutions found in literature [28]. In this subsection, the fiber volume is fixed to 0.47 (see Fig. 2). A tetrahedral conform mesh with quadratic elements is used and isotropic materials are considered. The fiber (boron) and the matrix (aluminum) are respectively denoted with a f and m index and have the following properties $E_f = 379.3$ GPa, $\nu_f = 0.1$ and $E_m = 68.3$ GPa, $\nu_m = 0.3$. Fiber axis is the direction 1.

The solution under Abaqus software is performed using the classical post-treatment method with the computation of the mean stress/strain whereas with SDT, effective properties are calculated with Eq. (10). Table 1 presents the estimated Engineering Constants, which validates the implementation.

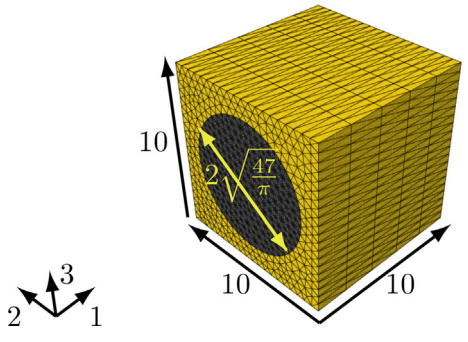

Fig. 2. RVE meshed with Abaqus with tetrahedral elements.

Table 1
Effective elastic properties for Boron/Aluminum composite (Vf = 0.47).

Engineering Constants	Abaqus	SDT	Hello [28]	VAMUSH [32]
E1 (GPa)	215.33	215.33	215.33	215.3
E2 = E3 (GPa)	143.98	143.98	143.96	144.1
G12 = G13 (GPa)	54.38	54.38	54.38	54.39
G23 (GPa)	45.83	45.83	45.82	45.92
$\nu 12 = \nu 13$	0.195	0.195	0.195	0.195
$\nu 23$	0.255	0.255	0.255	0.255

2.3. Extension to viscoelasticity

In one dimension, linear viscoelasticity of a non-aging material can use time domain constitutive relations using the Boltzmann integrals [33]

$$\sigma(t) = \int_0^t E(t-\tau)\frac{d\varepsilon(\tau)}{d\tau}d\tau \tag{11}$$

where $E(t)$ is an axial relaxation modulus. Alternatively, the frequency domain model considers harmonic excitation $\varepsilon(t) = Re(\varepsilon(\omega)e^{i\omega t})$ at angular frequency ω, as typically used for sine testing in a Dynamic Mechanical Analysis (DMA), leading to harmonic stress and the ratio of first harmonics gives the complex modulus

$$\sigma(\omega) = E(\omega)\varepsilon(\omega). \tag{12}$$

The two representations can be shown to be equivalent using the Laplace-Carson transform [34]. The linear stress/strain relation Eq. (12) is characterized by a frequency and temperature dependent complex modulus [6]

$$E(\omega, T) = E' + iE'' = E'(1 + i\eta) \tag{13}$$

where E' is the storage modulus and E'' the loss (dissipative) modulus and η the loss factor given by $\eta = E''/E'$.

To describe the effect of temperature, the frequency/temperature superposition principle [6,7] is assumed to be sufficient here, so that one describes the modulus as a function of the reduced frequency $\omega_R = \alpha(T)\omega$ with $\alpha(T)$ a temperature dependent shift factor. In 3D, for an anisotropic viscoelastic material, each term of the constitutive matrix $[C]$ is assumed complex and frequency dependent thus generalizing the scalar expression Eq. (12)

$$\{\sigma(\omega)\} = [C(\omega)]\{\varepsilon(\omega)\} \tag{14}$$

with

$$C_{ij} = C'_{ij} + iC''_{ij} = C'_{ij}(1 + i\eta_{ij}). \tag{15}$$

Assuming a loss factor associated to each stiffness components is not usual, and the only way to implement it in Abaqus is to develop a Umat subroutine. But this is consistent with the assumption that stress and strain are related by a linear time invariant multiple input/-multiple output transfer function.

Simplified forms exist in the presence of material symmetries. In the special case of isotropic material, Hooke's law can be expressed as

$$\begin{aligned}
[C] &= \begin{bmatrix} 2\mu+\lambda & \lambda & \lambda & 0 & 0 & 0 \\ & 2\mu+\lambda & \lambda & 0 & 0 & 0 \\ & & 2\mu+\lambda & 0 & 0 & 0 \\ & & & \mu & 0 & 0 \\ & & & & \mu & 0 \\ \text{symm.} & & & & & \mu \end{bmatrix} \\
&= \mu \begin{bmatrix} 2 & 0 & 0 & 0 & 0 & 0 \\ & 2 & 0 & 0 & 0 & 0 \\ & & 2 & 0 & 0 & 0 \\ & & & 1 & 0 & 0 \\ & & & & 1 & 0 \\ \text{symm.} & & & & & 1 \end{bmatrix} + \lambda \begin{bmatrix} 1 & 1 & 1 & 0 & 0 & 0 \\ & 1 & 1 & 0 & 0 & 0 \\ & & 1 & 0 & 0 & 0 \\ & & & 0 & 0 & 0 \\ & & & & 0 & 0 \\ \text{symm.} & & & & & 0 \end{bmatrix}
\end{aligned} \tag{16}$$

which uses the two complex and frequency/temperature dependent Lamé parameters $\lambda(\omega, T)$ and $\mu(\omega, T)$ and two constant real matrices.

Using engineering constants $\lambda = \frac{E\nu}{(1+\nu)(1-2\nu)}$ and $\mu = \frac{E}{2(1+\nu)}$, the non-linear dependence on the Poisson's ratio ν makes things more difficult and the classical approach is to only consider a scalar $E(\omega, T)$ with ν real and constant leading to

$$\begin{aligned}
[C] &= E[C^u] \\
&= E \begin{bmatrix} A+2B & A & A & 0 & 0 & 0 \\ & A+2B & A & 0 & 0 & 0 \\ & & A+2B & 0 & 0 & 0 \\ & & & B & 0 & 0 \\ & & & & B & 0 \\ \text{symm.} & & & & & B \end{bmatrix}
\end{aligned} \tag{17}$$

where $A = \frac{\nu}{(1+\nu)(1-2\nu)}$ and $B = \frac{1}{2(1+\nu)}$ are non-linear functions of ν and thus often considered constant. Some experimental studies [35–37] consider a dependence of ν on frequency and temperature and thus a ratio of transfers. This is not as direct as the assumption made here of a multi-variable transfer with frequency and temperature dependent coefficients. The choice of a E, ν parametrization is thus not practical if ν is not assumed real and constant.

For any anisotropic materials, the constitutive law can be expressed as a weighted sum

$$\begin{aligned}
[C] &= C_{11} \begin{bmatrix} 1 & 0 & 0 & 0 & 0 & 0 \\ & 0 & 0 & 0 & 0 & 0 \\ & & 0 & 0 & 0 & 0 \\ & & & 0 & 0 & 0 \\ & & & & 0 & 0 \\ \text{symm.} & & & & & 0 \end{bmatrix} + \ldots + C_{66} \begin{bmatrix} 0 & 0 & 0 & 0 & 0 & 0 \\ & 0 & 0 & 0 & 0 & 0 \\ & & 0 & 0 & 0 & 0 \\ & & & 0 & 0 & 0 \\ & & & & 0 & 0 \\ \text{symm.} & & & & & 1 \end{bmatrix} \\
&= \sum_{ij} C_{ij}\left[C^u_{ij}\right]
\end{aligned} \tag{18}$$

where the complex C_{ij} is the ij^{th} component of the stiffness matrix tensor and matrix $\left[C^u_{ij}\right]$ is a constant real matrix with the only nonzero components having the same ij indices as the coefficient.

The interest of this decomposition of the constitutive law is that it directly translates into the expression of the finite element complex stiffness matrix $[K] = [K(C')] + i[K(C'')] = [K'] + i[K'']$ as a linear combination with frequency and temperature dependent coefficient C_{ij} of constant real matrices associated with unit constitutive contribution $\left[C^u_{ij}\right]$

$$[K(\omega, T)] = \sum_{ij} C_{ij}(\omega, T)\left[K(C^u_{ij})\right] \tag{19}$$

For viscoelastic homogenization, the work equality is still used. The meaning is however slightly different since in a harmonic forced response, one distinguishes the elastic and dissipated work over a cycle.

The work W_{elas} of elastic forces can be expressed as a function of the storage moduli which are the real part of C^m. It corresponds to the integral over the volume of elastic forces at each material point and can be written as

$$2W_{elas}(q_k^h, q_l^h) = \{q_k^h\}^H [K'] \{q_l^h\} \tag{20}$$

where ^{H} means Hermitian (complex conjugate transpose). The dissipated work is related to the work of viscous forces within the volume over a cycle. It can be expressed as a function of the imaginary part of C^m as

$$W_{diss}(q_k^h, q_l^h) = \pi \{q_k^h\}^H [K''] \{q_l^h\} \tag{21}$$

The heterogeneous solution given by Eq. (7) is now complex since K^h is complex, and the homogenized properties are simply obtained as

$$[C^m]_{6\times 6} = \frac{[q^h]^H ([K'] + i[K'']) [q^h]}{|V|} \tag{22}$$

From the complex constitutive law $[C^m]$, getting the complex engineering constants is not obvious since as mentioned in earlier, the dependence on the Poisson's ratio are non-linear, so that conserving the elasticity relations as in [38,39] may not be a correct solution. Furthermore, the use of SUBC leads to the complex compliance matrix and an inverse operation, that may be source of error, is needed in order to get the stiffness matrix [40].

2.4. Viscoelastic benchmark

Loss factor computations are here compared to the results of Chandra [41] and Rezaei [42]. The RVE considered is a cylindrical inclusion in a rectangular cuboid of dimension $10 \times 10 \times 2$ mm. The fibre and the matrix are considered isotropic viscoelastic with the following properties $E_f = 72.4$ GPa, $G_f = 30.2$ GPa, $\nu_f = 0.2$, $\eta_f = 0.18\%$ and $E_m = 2.76$ GPa, $G_m = 1.02$ GPa, $\nu_m = 0.35$, $\eta_m = 1.5\%$. The boundary conditions used are PBC as in the publication of Rezaei [42].

For a volume fiber of 30%, the results shown in Table 2 have a maximum numerical difference of 7% in the axial direction with Rezaei and are very close to those of Chandra.

2.5. Application to 3D woven composite

At the yarn level (microscopic), which corresponds to the first scale, isotropic transverse elastic fiber and isotropic viscoelastic matrix are considered. A RVE consisting in an hexagonal arrangement (fiber packing) is used (see Fig. 3). According to [43], hexagonal arrayed fibers provide effective properties very close to randomly distributed fibers.

At the microscale, a conform mesh is used. It is generated by a 2D mesh cut by a level-set and then extruded in direction 3 (z) which corresponds to the axis fiber. The number of elements in this direction is fixed to 2 and has no influence on the homogenization.

The convergence study performed on this conform mesh shows that a refined mesh has no effect on the final result if the volume fraction of each constituent is constant. Indeed, for homogenization computation, the main influential factor is the accuracy on geometry. The mesh shown in Fig. 3 is used to perform the homogenization of the yarn using linear elements. In order to have accurate results, the volume fraction of each component is checked. The fiber volume fraction is set to 79% in the yarn.

Table 2
Comparison of loss factors for a cylindrical inclusion for a volume fiber of 30%.

VF	30%		
	SDT	Chandra [41]	Rezaei [42]
η_{11} (%)	0.30	0.31	0.28
η_{22} (%)	1.49	1.48	1.43
η_{12} (%)	1.49	1.48	1.46
η_{23} (%)	1.48	1.47	1.43

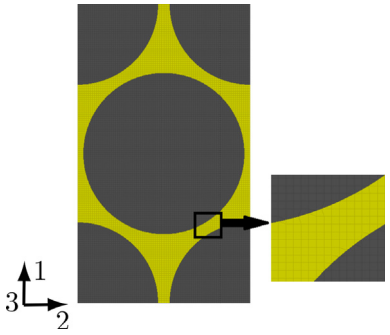

Fig. 3. Conform mesh for microscale.

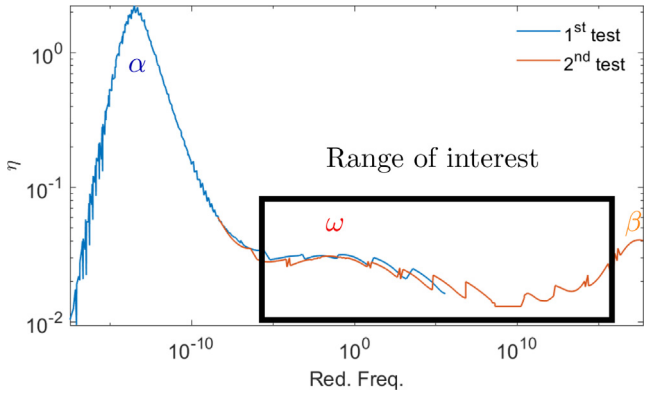

Fig. 4. Behavior of the matrix.

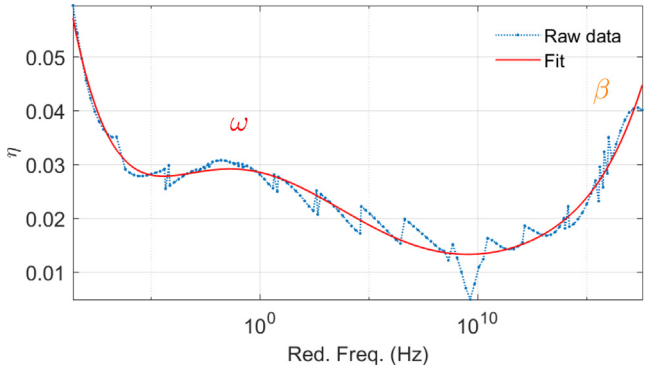

Fig. 5. Fit of matrix loss factor η in the range of interest.

A DMA is used to characterize the matrix behavior. For a temperature in the $[-40; 120]$ °C range, and a frequency in the $[50, 300]$ Hz range, which correspond to the range of interest, Fig. 4 illustrates that the matrix loss factor has important variation. The jerky effect observed is assumed to be linked to test machine stabilization problems for stiff and lightly damped material. However, the results are repeatable.

The area of interest is located on the ω transition just before the β transition [44,45], that is why the loss factor decreases from −40 °C to 0 °C (β transition), then increases to 100 °C and slightly decreases to 120 °C (ω transition). These transitions are known to appear for some epoxy/amine networks, and are mainly due to local movements at the molecular scale.

In order to get a continuous curve to model the matrix behavior, experimental data are fitted in Fig. 5 with a 6^{th} order polynomial.

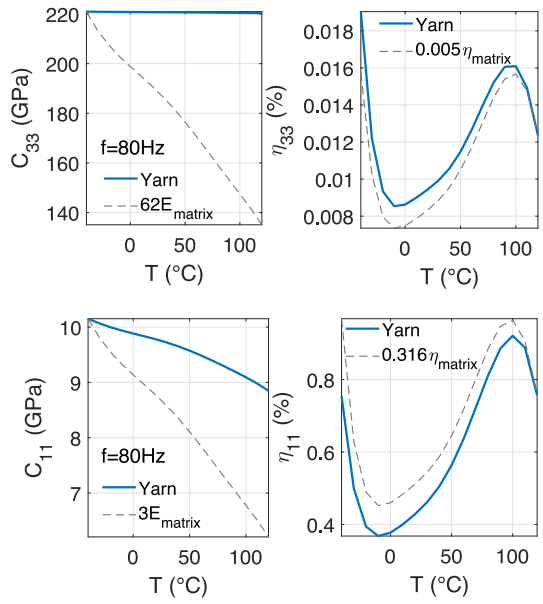

Fig. 6. Yarn storage modulus and loss factor at 80 Hz as a function of temperature for the longitudinal C_{33} and transverse C_{11} and its associated loss factor at micro-scale.

For a fixed frequency of 80 Hz, the fit of the matrix loss factor has a Pearson correlation coefficient $R^2 = 0.87$.

Fig. 6 shows the results in longitudinal (3) and the transverse (1) direction of the homogenization at the microscale obtained with periodic boundary conditions. In the longitudinal direction, the modulus does not depend on the matrix behavior and the damping is very low. The matrix behavior shown as a dashed line with a constant scale factor indicates that the modulus variation is much larger in the matrix than in the homogenized material, which is consistent with a very low damping.

In the transverse direction, the modulus is notably more sensitive and as expected this translates in notably higher damping. The loss factor evolution is similar to that of the matrix but the ratio is not constant. This is an indication of a microstructure effect, with the strain energy ratio in different constituents changing with temperature.

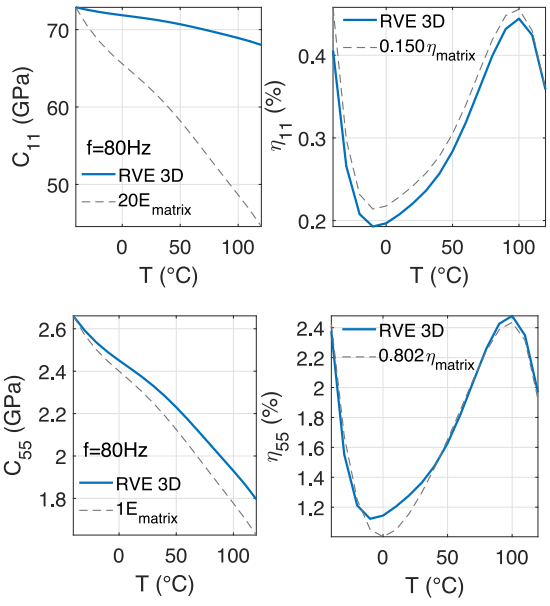

Fig. 7. 3D woven composite storage modulus C_{11} and C_{55} and its associated loss factor as function of temperature.

At the mesoscale, a voxel mesh shown in Fig. 1 with linear elements is used. For voxel meshes, geometric accuracy, which controls homogenized properties, depends on voxel size. Here the retained size is 100 μm, which corresponds to around 5 elements in the minor axis of the tow and was found to be a reasonable trade-off between cost and accuracy.

After the homogenization performed at the microscale, an isotropic transverse viscoelastic behavior is estimated for the yarns. The result is used at the mesoscale and combined with matrix volumes between yarns, in order to compute the homogenized viscoelastic properties of a 3D woven composite presented in Fig. 7).

At the mesoscale, the modulus is notably influenced by matrix properties. The warp direction is direction 1, the weft direction 2 and weft/warp shear is component 55 of the constitutive law. The matrix influence is more important in the shear direction because the modulus is lower and more sensitive to temperature and this translates into a higher loss factor. As for the microscale, the first order influence on the loss factor is the trend on the matrix. But the ratio between matrix and macroscale modulus is not perfectly constant, which indicates that energy contributions of the various constituents evolve slightly with the drop of matrix modulus at higher temperatures.

3. Validation of scale separation hypothesis

The next question is the validation of the scale separation assumption. Since the weaving pattern has a scale of a few centimeters that is close to characteristic dimensions of the structures thickness and characteristic stress gradient lengths, the assumption is not obvious. This will be pointed out during the experimental validation performed in Section 4.

3.1. Theoretical development

To determine the validity domain of the homogenized model, it is necessary to obtain an exact solution without the RVE edge effects that are present in the considered homogenization methods. For a geometrically periodic medium, which means a cell repeated indefinitely in space, an exact solution without discontinuity on the cell edges can be computed for all wavelengths using a model of size equal to two times the number DOF of the repeated cell [23,24]. Varying the wavelength of such exact solutions independently of the RVE dimension, gives a way to test the homogenized model validity as a function of wavelength and thus control the scale separation assumption.

A trivial approach would consider an arbitrary propagating wave in the homogeneous medium

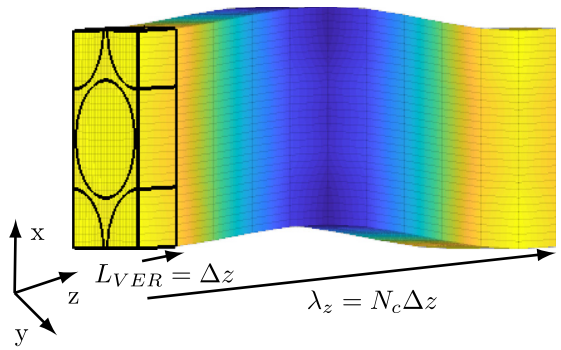

Fig. 8. Wavelength propagation in z direction at microscale.

$$
\begin{aligned}
[u^d(\kappa,X)] &= [\left\{u^d(\kappa,X)_j\right\}] \\
&= \Re(e^{i\{\kappa\}\{X\}})\begin{bmatrix}1&0&0\\0&1&0\\0&0&1\end{bmatrix} \\
&= \Re(e^{i\{\kappa\}\{X\}})[\{I_j\}]
\end{aligned}
\tag{23}
$$

with j index corresponding to the j^{th} displacement direction, $\{X\}=\{x,y,z\}^T$ the space position of a point inside the RVE and $\{\kappa\}=\{k_x,k_y,k_z\}^T$ representing wave number vector characterizing the propagation direction and of modulus giving the wavelength λ by

$$
\|\kappa\| = \frac{2\pi}{\lambda} \tag{24}
$$

Fig. 8 illustrates a shear wave with direction x displacement propagating in direction z (that is with $k_x=k_y=0$). The solid surface is the cell model and the wire frame illustrates restitution over multiple cells of a period. A compression wave would be motion in direction z propagating in direction z. It is however useful to note that propagation in oblique directions could also be considered.

Enforcing displacement in the heterogeneous medium however does not allow for the fluctuations expected at small scales and, as expected, the resulting strain energy is quite different from that of the homogeneous medium. The proposed alternative is to apply a periodic volume loading.

A first choice is to consider a propagating volume load equivalent to the shape of the displacement field as $\{f_v\}\equiv\left\{u_j^d\right\}$ which in a FEM model corresponds to the discretized load

$$
\{F_v(\kappa)\} = \frac{1}{\rho^m}[M^m(\rho^m)]\left\{q^d(\kappa)_j\right\} \tag{25}
$$

where values at mesh degrees of freedom are obtained as analytic value at nodes $\left[\left\{q^d(k_z,X)_j\right\}\right]=\left[\left\{u^d(k_z,X)_j\right\}\right]_{|nodes}$, ρ^m is the density of the homogenized medium and $[M^m(\rho^m)]$ is the homogenized mass matrix associated.

Note that the above expression, is independent of ρ_m, and gives a field in $length^4$ units and a unit scaling is used to obtain Newtons.

A second choice is to consider the volume load in equilibrium with a chosen displacement wave propagating in the homogeneous medium, in other words $f_v(\kappa,X)=\mathrm{div}\left([C^m]\left\{\varepsilon^d(\kappa,X)_j\right\}\right)$, which is more easily computed using

$$
\left\{F_v(\kappa)_j\right\} = [K^m]\left\{q^d(\kappa)_j\right\} \tag{26}
$$

Working in a quasi-static regime, the inertia terms are neglected. Thus, given a choice of $\left\{F_v(\kappa)_j\right\}$, the static periodic response $\left\{q(\kappa)_j\right\}$ is computed [23,24].

As in Eqs. (20) and (21) respectively, the stored energy is characterized by $\left\|\left\{q_j\right\}\right\|^2_{[K']}=\left\{q_j\right\}^H[K']\left\{q_j\right\}$ and the dissipated energy by $\left\|\left\{q_j\right\}\right\|^2_{[K'']}=\left\{q_j\right\}^H[K'']\left\{q_j\right\}$. To check the validity of the homogenized properties, two indexes are defined, one for the stored energy

$$
\frac{E^h_{elas}}{E^m_{elas}} = \frac{\left\|\left\{q^h_j\right\}\right\|^2_{[K'^h]}}{\left\|\left\{q^m_j\right\}\right\|^2_{[K'^m]}} \tag{27}
$$

and one for the dissipated energy

$$
\frac{E^h_{diss}}{E^m_{diss}} = \frac{\left\|\left\{q^h_j\right\}\right\|^2_{[K''^h]}}{\left\|\left\{q^m_j\right\}\right\|^2_{[K''^m]}}. \tag{28}
$$

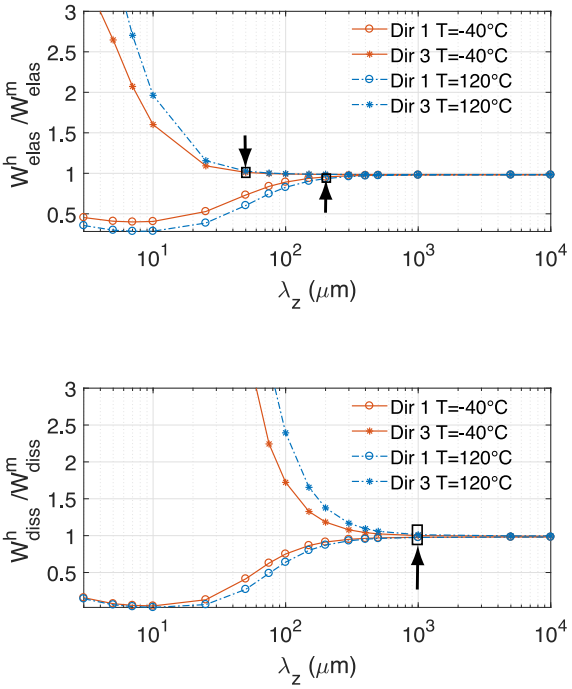

Fig. 9. Ratio between elastic (up) and dissipated (down) energy of the heterogeneous and homogeneous model for a yarn with a volume fiber of 75%.

Both should tend to one when the homogenized model is valid. Indeed, for high wave length, which means without stress gradient within the RVE, the energies of the two media are equal and scale separation hypothesis is verified.

An objective limit can be given by setting a threshold on previous indexes in order to have respectively information on the homogenized storage modulus and loss factor.

3.2. Verification at micro and meso scale

The microscale corresponds to the fiber scale, here, long continuous fibers composites are considered, therefore due to the yarn weaving the gradient of solicitation is expected to appear more in the longitudinal direction of the yarn than in the transverse one. To be confident in the homogenized value computed, the verification is performed by propagating a wave in the fiber direction which correspond to the direction z as shown Fig. 8. Indeed, it is the most disadvantageous direction of the RVE because it is the smallest with 1 μm, furthermore, for long fiber composites a RVE with this dimension doesn't represent well the fiber inside the yarn; whereas in the transverse direction fiber are fully represented.

Fig. 9 shows that compression (longitudinal, direction 3) waves have less than 2% elastic energy error for wavelengths above $\lambda_z=40$ μm. For shear waves (direction 1 and 2), the curves are identical and the 2% error only occurs below $\lambda_z=200$ μm. Convergence in the axial direction is thus faster and the most penalizing wave is shear. For the dissipated energy, convergence is slower. The wave nature does not seem to have influence on the range of validity. Indeed, for shear and compression waves, with the same 2% error margin, the homogenized loss factor is valid for $\lambda_z=1000$ μm. Moreover, the elastic and the dissipated energy inside the heterogeneous is overestimated for compression waves whereas it is the opposite for transverse waves. Finally, one can note that higher material contrast leads to slower convergence. Indeed, at -40 °C, the matrix is stiffer than at 120 °C, so its properties are closer those of the fiber.

For a wave propagation in the transverse direction (1 or 2), and loading given by Eq. (25), the convergence is reached for wavelength above 30 μm, implying that the homogenization is valid for any type of waves.

These observations show that the viscoelastic homogenization of the yarn is valid if the wavelength of the solicitation is higher than 1 *mm* in the targeted temperature range. Therefore, homogenized yarn properties can be used with confidence to perform mesoscale computations.

Similar computations will be shown in Section 4 for the mesoscale, since it can then be used to analyze validity of a finite model. Overall, the same trends as the microscale can be observed regarding the effect of the temperature, overestimation of energy in the heterogeneous medium for compression waves and slower convergence of dissipated energy.

4. Experimental identification of damping properties of 3D woven composites in temperature

To characterize modal damping of 3D woven composites specimens as a function of temperature, a modified Oberst test is considered. Focus is placed on the two first bending modes. The finite element model of this test is analyzed and shown to have imperfect scale separation, which may explain part of the small discrepancies between test and prediction.

4.1. Experimental setup

The validation experiment used here, and illustrated in Fig. 10, seeks to use relatively short 3D woven composite samples to characterize damping at low frequencies (a point needed below 100 Hz because it corresponds to the first bending mode of fan blades) and in the $-40\,^{\circ}$C to 120 $^{\circ}$C temperature range. The 200 mm sample length constraint answers the need to cut samples with repetitions and multiple orientations from a single test panel. But considering that a sufficient number of plies is needed to be representative of actual weaving, the resulting thickness varies from 4 to 12 mm.

Characterizing damping at low frequencies requires both a clamped free boundary condition and the addition of a significant top mass shown in Fig. 10. It is well known that clamping, tends to induce friction damping. Significant efforts were developed to minimize these effects. Thus a small contact surface was used and significant torque was applied to obtain high contact pressures. For thick samples, narrow 14 mm beams were preferred to the nominal 21 mm to obtain bending at lower frequencies. Finally amplitude/torque characterizations were used to estimate the damping added by such imperfect boundary conditions. Several investigations were made on the screw connection and power of the signal excitation in order to obtain a trade-off between signal to noise ratio and added friction damping.

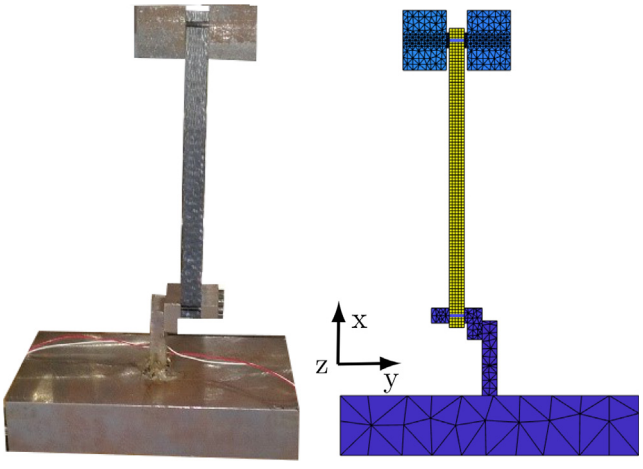

Fig. 10. Test bench and associated FE model.

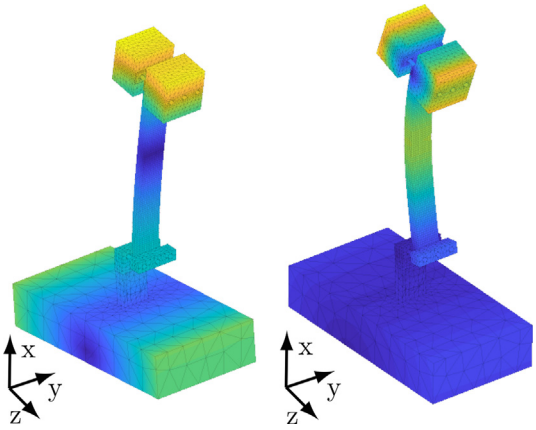

Fig. 11. Shape of the two first bending modes.

To avoid additional dissipation, the bending support is welded on a large steel block mounted on metallic springs. Permanently glued piezoelectric patches are used for both excitation and sensing allowing precise tracking of vibration properties when placing the bench in an environmental chamber. Finally, to estimate remaining bench induced damping, metallic specimens were tested both on the bench and in free-free conditions.

4.2. Pretest analysis of the FE model

The finite element model of the bench has been computed using SDT. Fig. 11 shows the first two modes which are bending modes.

In order to show the energy contribution of each component of the constitutive law, a simultaneous decomposition of the real and imaginary parts of the constitutive law is to obtain a series of 6 rank one energy contributions

$$C = \sum_{i=1}^{6} C_i = \sum_{i=1}^{6} \{\varepsilon_i\}\sigma_i\{\varepsilon_i\}^H \tag{29}$$

with principal values σ_i being complex, and left and right singular vectors $\{\varepsilon_i\}$ being equal and real because the matrix is symmetric. Naming of the contributions is based on the largest components of ε_i. Thus C_l is associated with the $\{\varepsilon_i\}$ whose largest component is in direction 11; C_{ti} with $i \in [1,2]$ is related to the component with 22 and 33 term and C_{xz} is the shear component C_{55} in the Eq. (18).

Fig. 12 shows the elastic and dissipated energy from the longitudinal, transverse and shear components.

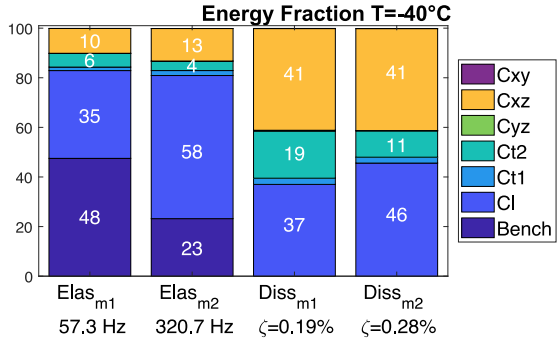

Fig. 12. Strain and dissipated energy fraction at $-40\,^{\circ}$C for mode 1 and 2.

It appears that the percentage of elastic energy from the bench and the bonds is significant, but these parts are considered purely elastic and thus their dissipated energy is zero. For the first and the second mode of a test specimen of 9.52 mm thickness, the energy fraction from the bench represent respectively 48% and 23% at a temperature of −40 °C thus the measurement for mode 2 should give a better characterization of the composite.

The second visible aspect is that C_{xz} contributes much more to damping dissipated than to stored energy. Indeed, for mode 1 at 57.3 Hz, the stored energy fraction for C_{xz} is 10%, while dissipated energy represents 41% of total. This results from the fact that the loss factor of this constitutive component is notably more damped than the axial component as shown in Fig. 7.

Due to confidential reasons, the properties and the weave pattern of the tested material are not those homogenized in Section 2.

It has been checked that the dissipated energy fraction shown in Fig. 12 corresponds to the weighting of elastic energy by that loss factor of each component. The modal strain energy approximation [46] estimating the modal damping ζ as

$$2\zeta = \eta = \sum_{ij} \eta_{ij} \frac{E(C'_{ij})}{\sum_{ij} E(C'_{ij})} \tag{30}$$

where $E_{C'_{ij}}$ is the elastic energy associated with component C'_{ij} of the constitutive law and $\eta_{C_{ij}}$ is the associated loss factor.

The dissipated energy computations, and the measured damping ratio, give a global quantification of damping. Visualizing where this energy gets dissipated is also important. Fig. 13 shows that the stress distribution in the sample for each bending modes differs for each constitutive components.

For the C_{xx} component, the distribution is for both modes well distributed along all the test specimen and a wavelength of 150 mm can be estimated. The length of the yellow stress concentration zone is 26 mm for the first mode and 40 mm for the second. For the C_{xz}, component, the first mode stress is concentrated near jaws with a zone of 10 mm; while the second mode shows concentrations in a 10 mm area at the top and 6 mm area at the bottom. These zones are smaller than the RVE size, so that the scale separation assumption is not obviously verified.

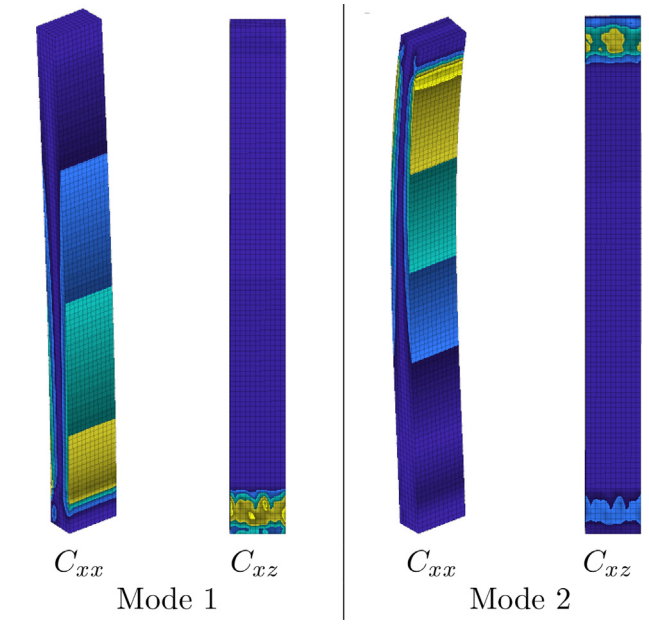

Fig. 13. Strain energy distribution for the two first bending modes at −40 °C regarding the contribution of the component C_{xx} and C_{xz}.

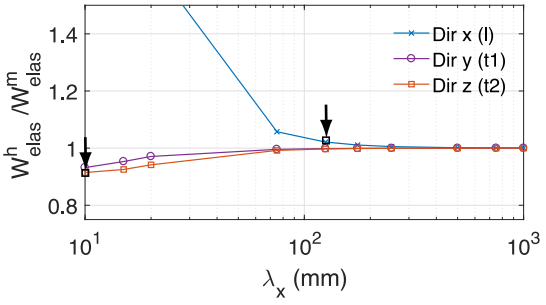

(a) Index for the stored energy

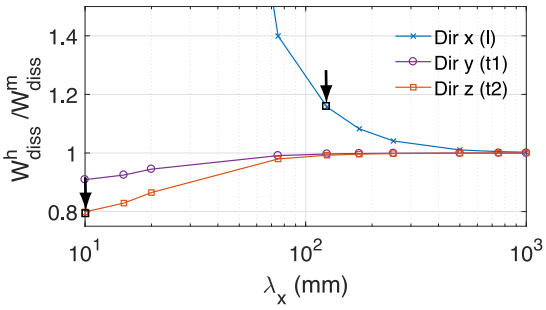

(b) Index for the dissipated energy

Fig. 14. Ratio between stored and dissipated energy of the heterogeneous and homogeneous model for a 3D woven composite for a direction of propagation in direction x.

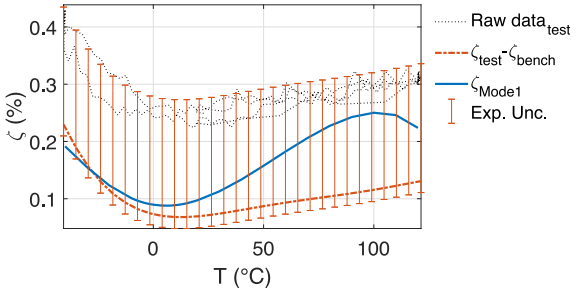

Fig. 15. Results of the simulation vs. test for mode 1.

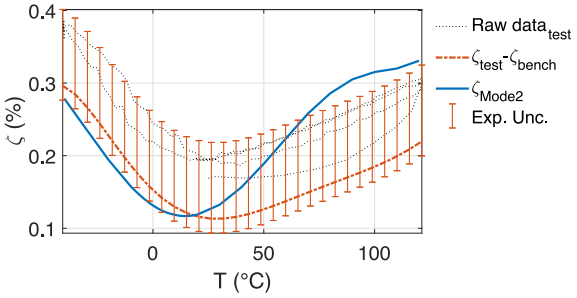

Fig. 16. Results of the simulation vs. test for mode 2.

Fig. 14, uses the criteria introduced in Section 3, but focuses on x propagation at small wavelength. The plot colors correspond to those used in Fig. 12.

For C_{xx} component, which has the highest contribution according to Fig. 12, one looks for x wave propagating in the x direction and

wavelengths of 150 mm as seen in Fig. 13, and finds a 2% error for the storage modulus shown by an arrow in Fig. 14a and a 15% error for the loss factor in Fig. 14b.

For the component C_{xz}, one considers wavelengths of 10 mm for a vertical wave 3 (z) propagating in the x direction, the figure show 9% error on storage modulus and 20% on loss factor. These observations can explain part of the difference between the test and simulation results.

4.3. Comparison

For the temperature range of interest, $[-40\ 120]$ °C, specimens cut in the warp direction (length direction) were tested and modal damping of the first two modes are shown in Figs. 15 and 16 respectively. The raw test result is represented by a dotted line. The dash-dot line represents the retained fit and an error bar is added to represent the variations in the measurement and an additional bench damping. The bench damping values, $\zeta_{bench} = 0.18\%$ for mode 1 and $\zeta_{bench} = 0.08\%$ for mode 2, are derived from comparison of free/free and bench test of metallic materials. Finally, the thick solid line represents the numeric results at the corresponding frequency.

The absolute level of predicted damping is very satisfactory for both modes. For the first mode, bench damping is actually higher than the composite sample contribution, but the composite values could be confirmed independently from full blade tests (not discussed in this paper).

The next feature to be predicted is the damping change with temperature, which presents a minimum in both test and analysis. The minimum is reached at 15 and 26 °C for the test and 6 and 15 °C in the analysis. The analysis values are within 1 °C of the minimum matrix damping using temperature/frequency equivalence. An error of about 10 °C in the position of this minimum seems quite plausible considering experimental difficulties in characterizing the matrix using frequency/temperature equivalence and the possible modification of its properties during the manufacturing process.

In the composite test, the ω transition (bump near 100 °C in the simulation) does not appear, with two plausible explanations. First Ref. [44] states that transition exists only for some specific epoxy materials and appears only in the initial state. In other words for an aged epoxy, this transition does not exist contrary to the β and α transitions. Second, imprecisions in the frequency/temperature equivalence used to predict matrix properties may play a role, since characterization was not perfect as discussed earlier.

The last feature is the extent of damping variations, about 0.16% for the first mode and 0.21% for the second for the simulation and respectively 0.16% and 0.18% for the experiment. These values are quite similar in test and analysis which is satisfying.

5. Conclusion

This paper proposed a numerical approach for viscoelastic homogenization. Assuming a viscoelastic behavior for the matrix, yarn and weave scales were considered successively and confrontation with experiment on a modified Oberst test bench was good in both absolute value and trends in temperature.

Matrix formulations allowed the simple use of model reduction methods leading to a procedure that is numerically efficient for temperature studies.

The methodology allowed detailed analysis of trends. First, the variations with temperature of the homogenized damping properties are, as expected, showing the same trends than the matrix with different transition temperatures affecting the response. But various components, corresponding to orientation and nature of loading, of the homogenized properties show significantly different damping levels and sensitivity to temperature. The usual correlation between high damping and high sensitivity to temperature is observed.

For predictions at the structure level, stored and dissipated energy were analyzed for principal components of the constitutive law and clearly demonstrated the presence of gradients at scales close to the RVE size. A verification strategy for the scale separation hypothesis using periodic computations provided an objective measure of accuracy for both storage moduli and loss factor. For the composite considered in the test, scale separation is improperly verified and could results in errors of up to 20% for the loss factor. Future steps, will be the consideration of a structural zoom near the jaw to verify the impact of the improper scale separation even though damping predictions are already quite satisfactory.

While these homogenization errors might explain some of the differences between test and analysis, it can be noted that the predicted damping minimum shifts of about 20 °C between matrix and composite tests and that the ω transition does not appear within the tested temperature range of the composite. Change of the matrix chemistry or inaccuracies in the measurement of matrix properties are plausible causes of theses differences that will need further investigation.

CRediT authorship contribution statement

Florian Conejos: Investigation, Conceptualization, Writing - original draft, Software. **Etienne Balmes:** Conceptualization, Writing - original draft, Software. **Bastien Tranquart:** Writing - review & editing, Funding acquisition. **Eric Monteiro:** Investigation, Writing - review & editing. **Guillaume Martin:** Investigation.

Declaration of Competing Interest

The authors declare that they have no known competing financial interests or personal relationships that could have appeared to influence the work reported in this paper.

References

[1] Chandra R, Singh SP, Gupta K. Damping studies in fiber-reinforced composites – a review. Compos Struct 1999;46(1):41–51.
[2] Treviso A, Genechten BV, Mundo D, Tournour M. Damping in composite materials: Properties and models. Compos Part B Eng 2015;78:144–52.
[3] Romano M, Ehrlich I, Gebbeken N. Structural mechanic material damping in fabric reinforced composites: A review. Arch Mater Sci Eng 2017;88(1):12–41.
[4] Pathan M, Tagarielli V, Patsias S. Effect of fibre shape and interphase on the anisotropic viscoelastic response of fibre composites. Compos Struct 2017;162:156–63.
[5] Thierry V, Chronopoulos D. The impact of mesoscale textile architecture on the structural damping in composite structures. Compos Struct 2020;249:112475.
[6] Nashif A, Jones D, Henderson J. Vibration damping. John Wiley & Sons; 1985.
[7] Jones D. Handbook of viscoelastic vibration damping. John Wiley & Sons; 2001.
[8] Chen T. Determining a prony series for a viscoelastic material from time varying strain data. tech. rep. NASA Langley Technical Report Server 2000.
[9] Renaud F, Dion J-L, Chevallier G. Méthode d'identification des paramètres d'un modèle de Maxwell généralisé pour la modélisation de l'amortissement. Méc Ind 2010;11(1):47–55.
[10] Christensen RM. Viscoelastic properties of heterogeneous media. J Mech Phys Solids 1969;17(1):23–41.
[11] Hashin Z. Complex moduli of viscoelastic composites-I. General theory and application to particulate composites. Int J Solids Struct 1970;6:539–52.
[12] Hirsekorn M, Petitjean F, Deramecourt A. A continuous threshold model for the visco-elasto-plastic behavior of PET based multi-layer polymeric films. Mech Time-Depend Mater 2010;14(1):25–45.
[13] Courtois A, Marcin L, Benavente M, Ruiz E, Lévesque M. Numerical multiscale homogenization approach for linearly viscoelastic 3D interlock woven composites. Int J Solids Struct 2019;163:61–74.
[14] Rique O, Liu X, Yu W, Pipes RB. Constitutive modeling for time- and temperature-dependent behavior of composites. Compos Part B Eng 2020;184:107726.
[15] Bornert M, Bretheau T, Gilormini P. Homogénéisation en mécanique des matériaux 1: matériaux aléatoires élastiques et milieux périodiques. Hermes Science Publications; 2001.
[16] Lomov S, Huysmans G, Luo Y, Parnas R, Prodromou A, Verpoest I, Phelan F. Textile composites: modelling strategies. Compos Part A Appl Sci Manuf 2001;32(10):1379–94.

[17] Kanouté P, Boso D, Chaboche J, Schrefler B. Multiscale methods for composites: a review. Arch Comput Methods Eng 2009;16:31–75.
[18] Charalambakis N. Homogenization techniques and micromechanics. A survey and perspectives. Appl Mech Rev 2010;63.
[19] Saeb S, Steinmann P, Javili A. Aspects of computational homogenization at finite deformations: A unifying review from Reuss' to Voigt's Bound. Appl Mech Rev 2016;68(5)..
[20] Kanit T, Forest S, Galliet I, Mounoury V, Jeulin D. Determination of the size of the representative volume element for random composites: statistical and numerical approach. International Journal of Solids and Structures 2003;40(13):3647–79.
[21] Forest S, Sab K. Cosserat overall modeling of heterogeneous materials. Mech Res Commun 1998;25(4):449–54.
[22] Kouznetsova V, Geers M, Brekelmans W. Multi-scale constitutive modelling of heterogeneous materials with a gradient-enhanced computational homogenization scheme. Int J Numer Methods Eng 2002;54:1235–60.
[23] Mace B, Duhamel R, Brennan M, Hinke J. Finite element prediction of wave motion in structural waveguides. J Acoust Soc Am 2005;117:2835–43.
[24] Pinault H, Arlaud E, Balmes E. A general superelement generation strategy for piecewise periodic media. J Sound Vib 2020;469:115–33.
[25] Balmes E. Structural Dynamics Toolbox, user's guide. SDTools, 1995–2021..
[26] Mandel J. Contribution théorique à l'étude de l'écrouissage et des lois de l'écoulement plastique. In: Applied mechanics. Berlin, Heidelberg: Springer; 1966. p. 502–9.
[27] Hill R. The essential structure of constitutive laws for metal composites and polycrystals; 1967. p. 79–95..
[28] Hello G, Schneider J, Aboura Z. Numerical simulations of woven composite materials with voxel-FE models. In: 16th European conference on composite materials (ECCM), Seville, Spain, June 2014..
[29] Hazanov S, Amieur M. On overall properties of elastic heterogeneous bodies smaller than the representative volume. Int J Eng Sci 1995;33(9):1289–301.
[30] Zienkiewicz O, Taylor R, Zhu J. The finite element method: its basis and fundamentals. 6th ed.,. Butterworth-Heinemann; 2005.
[31] Balmes E. Parametric families of reduced finite element models. Theory and applications. Mech Syst Signal Process July 1996;10:381–94.
[32] Yu W, Tang T. Variational asymptotic method for unit cell homogenization of periodically heterogeneous materials. Int J Solids Struct 2007:3738–55.
[33] Lakes R, Vanderby R. Interrelation of creep and relaxation: a modeling approach for ligaments. J Biomech Eng 2000;121(6):612–5.
[34] Salençon J. Viscoélasticité. Paris: Presse des Ponts et Chaussés; 1983.
[35] Tschoegl NW. The phenomenological theory of linear viscoelastic behavior: an introduction. Berlin Heidelberg: Springer-Verlag; 1989.
[36] Pritz T. Measurement methods of complex Poisson's ratio of viscoelastic materials. Appl Acoust 2000;60:279–92.
[37] O'Brien DJ, Sottos NR, White SR. Cure-dependent viscoelastic poisson's ratio of epoxy. Exp Mech Apr. 2007;47:237–49.
[38] Pecker A. Dynamique des sols. presses de l'école nationale des ponts et chaussées ed.; 1984..
[39] Di Benedetto H, Delaporte B, Sauzéat C. Three-dimensional linear behaviour of bituminous materials: experiments and modeling. Int J Geomech 2007;7 (2):149–57.
[40] Hashin Z. Damping characteristics of fiber composites. tech. rep., Technion-Israel Inst. of Tech. Haifa Dept. of Materials Engineering; 1972..
[41] Chandra R, Singh SP, Gupta K. Micromechanical damping models for fiber-reinforced composites: a comparative study. Compos Part A Appl Sci Manuf 2002;33(6):787–96.
[42] Rezaei A, Goroz Gómez D, Gilabert F, Desmet W, Van Paepegem W. Micro-scale finite element simulation of the viscoelastic damping in unidirectional fiber reinforced composites. Leuven, Belgium: Katholieke Univ Leuven, Dept Werktuigkunde; 2016. p. 1757–66.
[43] Liu Y, Yan Y, Yang L, She H, He M. Prediction on macroscopic elastic properties of interphase-contained long-fiber-reinforced composites and multiple nonlinear regression analysis. J Reinforced Plast Compos 2012;31(17):1143–57.
[44] Ernault E. Thermo-oxydation de réseaux époxy/amine. PhD thesis. Paris: Arts et Métiers ParisTech - Centre de Paris; 2016.
[45] Delozanne J. Durabilité des époxys; application au collage structural aéronautique. PhD thesis, Arts et Métiers ParisTech - Campus de Paris, Paris; 2018..
[46] Rogers L, Johson C, Keinholz D. The modal strain energy finite element method and its application to damped laminated beams. Shock Vib Bull 1981;51..